Materials Research Bulletin 48 (2013) 3559–3563

Contents lists available at SciVerse ScienceDirect

Materials Research Bulletin

journal homepage: www.elsevier.com/locate/matresbu

Microstructure and magnetic properties of iron modified mesoporous silica obtained by one step direct synthesis

Natalia Cuello [a], Verónica Elías [a,c], Silvia Urreta [b], Marcos Oliva [b], Griselda Eimer [a,c,*]

[a] Centro de Investigación y Tecnología Química (CITeQ), Universidad Tecnológica Nacional, Fac. Reg. Córdoba, Maestro López esq. Cruz Roja Arg. Ciudad Universitaria, 5016 Córdoba Capital, Argentina
[b] IFEG-CONICET, FaMAF-Universidad Nacional de Córdoba, Córdoba, Argentina
[c] CONICET, Argentina

ARTICLE INFO

Article history:
Received 25 March 2013
Received in revised form 10 May 2013
Accepted 16 May 2013
Available online 24 May 2013

Keywords:
A. Magnetic materials
A. Nanostructures
B. Sol-gel chemistry
C. X-ray diffraction
D. Magnetic properties

ABSTRACT

Iron-containing MCM-41 molecular sieves have been successfully synthesized by directly incorporating the metal in the initial synthesis gel. The resulting microstructures were characterized by XRD, UV–vis DR, ICP and N_2 adsorption. Room temperature magnetic properties were evaluated by measuring the magnetization vs. applied magnetic field loops, up to 5 T. The results show that the structural, chemical and magnetic properties of the resulting materials strongly depend on the hydrothermal treatment time and the iron content. The hysteresis loops exhibit para-, superpara- and ferromagnetic contributions in agreement with the iron species distributions. It is found that longer hydrothermal treatments result in a stabilization of the iron into the network and in a refiner effect of the oxide particles.

1. Introduction

The fabrication routes of metal oxide nanoparticles, with different sizes and shapes have been extensively studied in recent years because of their potential application in many areas including device fabrication, solar cells, catalysis, sensors and fuel cells [1–3]. Among the nanoparticles, magnetic nano-sized iron oxides are very useful for many applications in biomedicine, magnetic memories and electronics [4,5]. The biomedic applications include magnetic bioseparation [6], biological labeling and diagnostics, enhancement of contrast agents for magnetic resonance imaging, hyperthermia of tumors and drug-carrier design [7–11].

The synthesis of magnetic nanoparticles with a quite small size is extremely difficult because the individual particles tend to aggregate and/or coalesce, losing the specific properties associated to non-interacting superparamagnetic particles. These problems can be overcome by fabricating nanoparticles in solid porous supports offering high surface area and large pore diameter, which inhibit agglomeration and enhance the stability of the metal and metal oxide nanoparticles [1–3,12,13].

Ordered mesoporous silicas (OMS) [14,15] such as MCM-41, have received much attention due to their superior properties of high surface area, large pore volume, uniform pore size in the range of 2–30 nm and tunable surface functional groups [15]. Several applications have been proposed in the fields of catalysis, adsorption and separation, lasers, sensors, solar cells, host-guest chemistry, biomedical chemistry and environmental technologies [16–22]. In this context, the synthesis of mesoporous nanocomposites having magnetic elements embedded in the nanochannels or inside the porous framework is very promising due their potential uses. In the biomedical field, these nanocomposites offer high loading of drug/bioactive agents as well as the ability of selectively deliver the drug in the desired organs or tissues inside the body, by the application of an external magnetic field [23–27].

Many synthesis methods for the preparation of iron-modified mesoporous silica materials have been investigated such as: (i) impregnation of iron precursors (e.g. iron salts as $Fe(NO_3)_3$) on previously synthesized mesoporous SiO_2 particles, followed by thermal and/or chemical treatment in order to produce magnetic nanoparticles, mainly magnetite or maghemite inside the porous structure [28–30]; (ii) coating of previously prepared Fe_3O_4 nanoparticles with mesoporous SiO_2, using a cationic or neutral surfactant as template [31–33]; (iii) reverse micro-emulsion

* Corresponding author at: Centro de Investigación y Tecnología Química (CITeQ), Universidad Tecnológica Nacional, Fac. Reg. Córdoba, Maestro López esq. Cruz Roja Arg. Ciudad Universitaria, 5016, Córdoba Capital, Argentina.
Tel.: +54 0351 4690585; fax: +54 0351 4690585.
E-mail addresses: geimer@scdt.frc.utn.edu.ar, griseeimer@yahoo.com.ar (G. Eimer).

0025-5408/$ – see front matter © 2013 Elsevier Ltd. All rights reserved.
http://dx.doi.org/10.1016/j.materresbull.2013.05.065

techniques [34,35]; (iv) aerosol or spray-drying techniques [36,37]; (v) self-assembling [38,39]; (vi) phase transfer method [40], among others. Using one of these methods, or a combination of them, it has been possible to prepare particles with diameters ranging from nanometric to micrometric dimensions, with tailored morphological and magnetic and textural properties according to the desired application. Moreover, depending on the preparation method used, the presence of isolated metal ions and/or highly dispersed metal oxide particles or coatings have been proven.

Many works describing the properties of magnetic mesoporous materials prepared by post-synthesis modifications [39,41–44] can be found in the literature. Among others, Surowiec et al. [41] studied the magnetic properties of MCM-41 type mesoporous silica modified by impregnation with iron and nickel salts. However, reports about the synthesis of these materials by direct methods are quite scarce. During the post-synthesis modification procedure, pore necking or blocking may take place. A good way to prevent pore blocking is then to include the magnetic species direct in the initial gel. In this work, we report the preparation of iron modified mesoporous silica by a direct synthesis method based on a sol–gel process and using a cationic surfactant as template. The influence of the iron content and the hydrothermal treatment time on the magnetic and microstructure properties of the mesoporous materials is investigated.

2. Experimental

The iron-containing MCM-41 type mesoporous materials were prepared by a direct hydrothermal method using cetyltrimethyl ammonium bromide (CTABr, Aldrich) as template. Tetraethoxysilane (TEOS, Fluka ≥ 98%) and ferric nitrate ($Fe(NO_3)_3{\cdot}9H_2O$, Aldrich ≥ 98%) were used as the Si and Fe sources, respectively. The pH of the synthesis was adjusted to 12 by adding a tetraethylammonium hydroxide (TEAOH, Fluka) 20 wt.% aqueous solution. The catalysts were synthesized from a gel of molar composition: Si/Fe = 20 and 60; TEAOH/Si = 0.3; CTABr/Si = 0.3; H_2O/Si = 60. In a typical synthesis, TEOS and iron salt were aggregated to a 20 wt.% solution of CTABr in water under agitation, and maintained for 30 min. Then, TEAOH was added drop wise and the mixture was then continuously stirred for 3 h. Finally, the water was further added, and the agitation kept constant for 15 min. This gel was filtered, washed with distilled water until pH ∼ 7 and dried at 60 °C overnight or treated hydrothermally into a Teflon-lined stainless-steel autoclave, kept in an oven at 100 °C for 1–5 days under autogeneous pressure. Again, the hydrothermally treated final solids were filtered, washed with distilled water until pH ∼ 7 and dried at 60 °C overnight. The template was evacuated from the samples by heating (2 °C/min) under N_2 flow (45 mL/min) at 500 °C for 6 h and then calcinated at 500 °C for 6 h under dry air flow (45 mL/min). The samples were named: Fe-M(*x*)*y* where *x* is the initial Si/Fe molar ratio and *y* are the days of the hydrothermal treatment.

3. Characterization

The X-ray diffraction (XRD) patterns of the samples were recorded in a Philips PW 3830 diffractometer with Cu Kα radiation (λ = 1.5418 Å) in the range of 2θ from 1.5° to 7° to confirm the MCM-41 structure and from 10° to 70° to detect possible crystalline oxide phases in the samples. The interplanar distance, $d_{1\,0\,0}$, was calculated, from the position of the first X-ray diffraction line and the lattice parameter (a_0) of the hexagonal unit cell was calculated as $a_0 = (2/\sqrt{3})\, d_{1\,0\,0}$. UV–vis diffuse reflectance (UV–vis DR) spectra were recorded using an Optronics OL 750-427 spectrometer in the wavelength range 200–600 nm. The Fe content was determined by Atomic Absorption spectroscopy (AA) using a Varian SpectrAA 220. Specific surface area was determined using a Micromeritics Pulse Chemisorb 2700. The room temperature magnetization vs. field curves were measured in a Quantum Design SQUID magnetometer MPMS XL7 with static field up to $\mu_0 H = 5$ T. The hysteresis properties as the coercive field and remanent magnetic moment were estimated from the magnetization loops; these curves were well fitted by the sum of three contributions: a linear paramagnetic or diamagnetic contribution (LM), a ferromagnetic one (FM) [45], and a superparamagnetic-like one (SPM) [46], so that the total magnetization results: TM = LM + FM + SPM, with

$$\mathrm{LM} = \chi \mu_0 H \tag{1}$$

$$\mathrm{FM} = \frac{2M_{\mathrm{SF}}}{\pi}\left(\tan^{-1}\left(\frac{H+\mu_0 H_{\mathrm{C}}}{\mu_0 H_{\mathrm{C}}}\right)\tan\frac{\pi M_{\mathrm{RF}}}{M_{\mathrm{SF}}}\right) \tag{2}$$

$$\mathrm{SPM} = M_{\mathrm{SS}}\left(\coth\frac{\mu_{\mathrm{SP}}(H_{\mu_0}+\mu_0 H^*)}{K_B T} - \frac{K_{\mathrm{B}}T}{\mu_{\mathrm{SP}}(H\mu_0+\mu_0 H^*)}\right) \tag{3}$$

Here $\mu_0 H_{\mathrm{C}}$, M_{SF} and M_{RF} are the coercive field and the effective saturation and remanent moments, associated to the ferromagnetic contribution, respectively. M_{SS}, μ_{SP} and $\mu_0 H^*$ are the effective saturation moment, the mean magnetic moment of the activated clusters and a mean interaction field, introduced to account for the effect of interactions between particles on the superparamagnetic-like component of the M(H) loops.

4. Results and discussion

4.1. X-ray diffraction

Table 1 summarizes the synthesis parameters and the microstructure properties of all the resulting materials. The XRD patterns of the samples prepared with different Si/Fe molar ratios in the synthesis gel and different hydrothermal treatment times are shown in Fig. 1. All the materials exhibit, besides an intense low-angle reflection at 2.3–2.7° corresponding to the distance between (1 0 0) planes, other two weak peaks at about 4.75° and 5.50° corresponding to reflections from (1 1 0) and (2 0 0) planes, typical of the MCM-41 mesoporous structure. In samples with a Si/Fe ratio of 60 (Fe-M(60)*y*, Fig. 1A), all these peaks gradually decrease in height, broaden and overlap when the synthesis time increases. These facts indicate that long hydrothermal synthesis times partially deteriorate the hexagonal pore structure order of the Fe-M(60)*y* solids [47]. In contrast, for the Si/Fe ratio of 20 (Fig. 1B), a quite notable improvement of the mesoporous arrangement is observed when the hydrothermal treatment time increases. In fact, at least two days of hydrothermal synthesis are required to obtain well ordered pore arrays in the MCM-41 structure, as it is evidenced by the three diffraction peaks in the XRD pattern of the Fe-M(20)2 sample. Even when opposite behaviors are found for different iron contents, all the materials

Table 1
Synthesis parameters and the physical properties of the synthesized solids.

Sample	Hydrothermal treatment time (days)	Si/Fe (initial molar ratio)	Area (m^2/g)	$d_{1\,0\,0}$ (nm)	a_0[a] (nm)
Fe-M(60)0	0	60	1850	3.20	3.74
Fe-M(60)1	1	60	1782	3.59	4.02
Fe-M(60)2	2	60	1482	3.80	4.32
Fe-M(60)5	5	60	1128	3.66	4.29
Fe-M(20)0	0	20	798	3.24	3.75
Fe-M(20)2	2	20	1189	3.57	4.12
Fe-M(20)5	5	20	1164	3.66	4.22

[a] $a_0 = (2/\sqrt{3})\, d_{1\,0\,0}$.

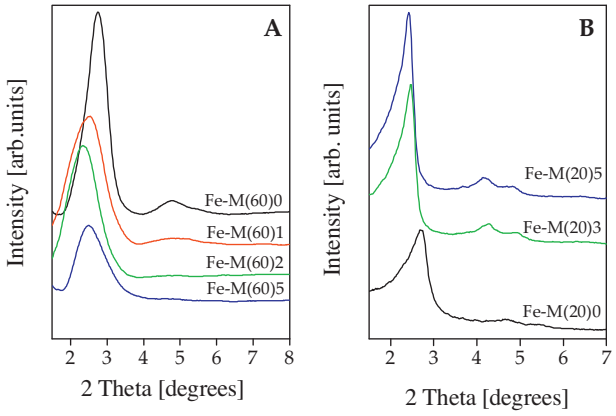

Fig. 1. XRD patterns of samples synthesized with different hydrothermal treatment times and Si/Fe molar ratios of: (A) 60 (~1.12 wt.%) and (B) 20 (~4.2 wt.%).

described here show a well defined mesoporous structure, stable under calcination, in contrast to the low structural order often reported [48] when direct synthesis methods are applied for introduce metal species in the mesoporous network.

Then, assuming a MCM-41 structure for all the samples, the lattice parameter (a_0) is calculated for comparative purposes (Table 1). Although the MCM-41 walls are amorphous, the lattice parameter a_0 is affected by the addition of elements different from Si and their changes are generally accepted as evidence of foreign elements incorporated into the silicate framework [49,50]. In general, the substitution of Si^{4+} by the larger iron ions distort the ideal Td geometry around the iron atom and this new length of Si–O–Fe bond, being different from that of Si–O–Si, should lead to some disorder in the pore arrangement. On the other hand, when the loaded Fe atoms form small clusters or particles filling the MCM-41 pores, some structure deformation is also expected. Then, for the Si/Fe ratio of 60, the increase in the parameter a_0 observed as the hydrothermal synthesis time increases is consistent with iron incorporated into the siliceous framework. In the case of the samples synthesized with higher Fe content (Si/Fe ratio = 20), the parameter a_0 also increases with the synthesis time besides that the structural order is notably enhanced (Fig. 1B). These facts give account for that when the Fe amount in the initial gel is high, this metal is successfully incorporated into the framework (replacing the Si^{4+} ions) while the quality of the mesoporous structure is improved. This is probably due to the formation of new Si–O–Si and Si–O–Fe bridges and additional network cross linking, which require longer synthesis times when the Fe content is high. On the other hand, the higher relative structural order found for the samples synthesized with higher Fe content, with respect to those synthesized with lower Fe content, could be also consistent with the formation of nanoparticles and/or nanoclusters on the external surface of the MCM-41 supports. It has been reported that for low metal contents, the clusters and oxide nanoparticles form inside the mesoporous. When the metal exceeds some critical concentration, particles also nucleate on the outer support surface [47,51]. These particles forming outside the pores are likely to grow during calcination at the expenses of those inside the pores, leading to the progressive improvement of the hexagonal pore array typical of MCM-41 detected by X-ray diffraction.

No characteristic diffraction peaks of iron oxide are detected in the wide-angle XRD pattern as if the iron-oxide species were amorphous or the crystal domain size below the XRD detection limit (<4–6 nm). Such species are likely to be finely dispersed in the silica structure inside the channels or on the external surface. In contrast with these results, larger particles of different iron species such as nano-crystals of metallic Fe^0, Fe_3O_4 and mainly Fe_2O_3 were detected by us [47] when mesoporous silica was impregnated with ferric nitrate, calcined and then treated under H_2 flow at high temperature.

Concerning the total specific surface of the samples investigated, most of them show values higher than 1000 m^2/g, characteristic of mesoporous structures. However, the smaller specific surface values observed for the samples synthesized with higher Fe content is according with the higher presence of oxides on the external surface, partially blocking the access to the mesopores. In samples with Si/Fe molar ratio of 60 the hydrothermal treatment causes a decrease in the specific surface in concordance with the loss of structural order evidenced by XRD. In change, for the Si/Fe molar ratio of 20 the specific surface increases with the hydrothermal treatment time also according to the improvement in the structure ordering.

4.2. UV–vis DR spectroscopy

The UV–vis DR spectroscopy is a useful method to characterize the coordination environment of transition metals in zeolite-type frameworks [52], so it is used here to corroborate that iron atoms are inserted into the silica network and that iron rich species can also be formed. The UV–vis DR spectra of the samples synthesized with Si/Fe initial molar ratios of 60 and 20 in the synthesis gel and with different hydrothermal treatment times are shown in Fig. 2. A strong absorption band in the 200–300 nm range with two maxima about 220 nm and 250 nm (overlapped in some cases) is associated with the $d\pi$–$p\pi$ charge transfer between Fe and O that is characteristic of isolated iron cations in tetrahedral coordination [52–54]. This indicates that iron is linked to the O atoms, being incorporated into the mesoporous framework through the formation of Si–O–Fe bonds. The contributions detected at longer wavelengths evidence that iron is also present with octahedral coordination in extra-framework positions. Thus, the absorption between 300 nm and 450 nm may be attributed to small oligonuclear clusters [52–55], while the broad band between 450 and 600 nm is considered to arise from iron oxide nanoparticles larger than the clusters [52,53]. Previous reports [56] indicate that bulk α-Fe_2O_3 exhibits a broad adsorption band between 320 and 670 nm, with a maximum at 560 nm; it is known that the UV bands shift to shorter wavelengths when the size of iron oxide nanoclusters or nanoparticles decreases, indicating a quantum size effect in these species [57]. It should be noted here that all the as-synthesized samples were white and their UV–vis DR spectra

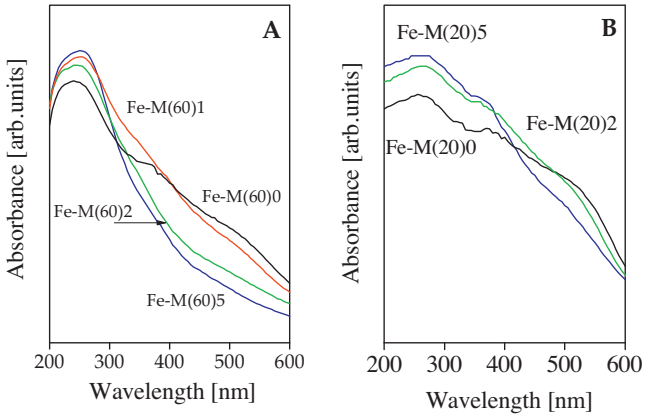

Fig. 2. UV–vis DR spectra of samples synthesized with different hydrothermal treatment times and Si/Fe molar ratios of: (A) 60 (~1.12 wt.%) and (B) 20 (~4.2 wt.%).

(not shown) exhibited a unique band at 200–300 nm, confirming that the iron cations were incorporated inside the framework during the hydrothermal synthesis. Moreover, the absence of bands above 300 nm also confirmed that neither clusters nor iron oxide nanoparticles were present. These facts indicate that the calcination process, applied to remove the template, causes the migration of the iron ions initially in tetrahedral coordination into framework toward the pore wall surface to form the clusters or the nanoparticles of iron oxides found after calcination. The higher absorption at longer wavelengths for the Fe-M(20)*y* samples is likely to be a consequence of the high iron content, promoting the major formation of iron oxide clusters and/or nanoparticles which could be mainly located on the external surface, judging by the lower area values and higher structural regularity of these samples. On the other hand, for both Si/Fe ratios, the time of hydrothermal treatment seems to favor the stabilization of the iron ions inside the mesoporous framework, decreasing their mobility during calcinations and subsequent segregation of oxides. This is evidenced by the decreased absorption at longer wavelengths and the increase in the intensity of the absorption at shorter wavelengths according the synthesis time increases (Fig. 2). These results are also in agreement with the calculated a_0 parameters. In particular, for the Si/Fe ratio of 60, the amount and size of iron oxides decrease with the synthesis time while the specific surface and structural regularity also decrease, indicating that the variation of these species, finely dispersed likely inside the mesopores, does not affect such structural parameters. Meanwhile, for the higher Fe content, the decrease in the size of the oxides, mainly located on the external surface, is according with the increase in the specific surface and structural regularity.

Finally, the percentage of iron incorporated in the samples with Si/Fe molar ratios of 60 and 20 was about 1.2 and 4.2 wt.%, respectively, independently of the nature of the metallic species present and the hydrothermal treatment time.

4.3. Magnetic properties

The iron modified MCM-41 mesoporous supports are expected to show different magnetic behaviors depending on the iron atoms distribution and the size of the iron containing species. The bare silica support is diamagnetic, metallic iron and some oxides are ferromagnetic, while the most stable oxide, hematite, is a canted antiferromagnetic material. Small particles of ferromagnetic materials, as those formed inside the pores, can show a superparamagnetic behavior, while larger particles grown on the outer surface are likely to behave as ferromagnetic. Meanwhile a paramagnetic behavior is expected for isolated iron ions into the matrix. Thus, the hysteresis loops of the samples investigated should show different contributions. Fig. 3 presents the fitted magnetization curves for the samples synthesized with Si/Fe molar ratios of 60 and 20 and different hydrothermal treatment times. In samples with Si/Fe ratio of 60 (Fig. 3A) the hysteresis loops show a dominant diamagnetic component due to the silicate framework. Moreover, samples without and with 2 days of hydrothermal treatment exhibit a very small ferromagnetic contribution which may be attributed to a few larger iron oxide species dispersed on the external surface of the silica [58–60]. After five days of treatment, a superparamagnetic contribution appears, indicating the formation of iron oxides smaller in size (under the critic size [58]) and located probably inside the pores. Hence, for the samples with lower Fe content (Si/Fe = 60), a longer thermal treatment increases the magnetic response due to the higher stabilization of iron into the framework with the consequent segregation of smaller size oxides (as it is evidenced by UV–vis RD), even when the Fe content remains practically unchanged (~1.12 wt.%). For an Fe content of 4.2 wt.% (samples with si/Fe ratio = 20) all the

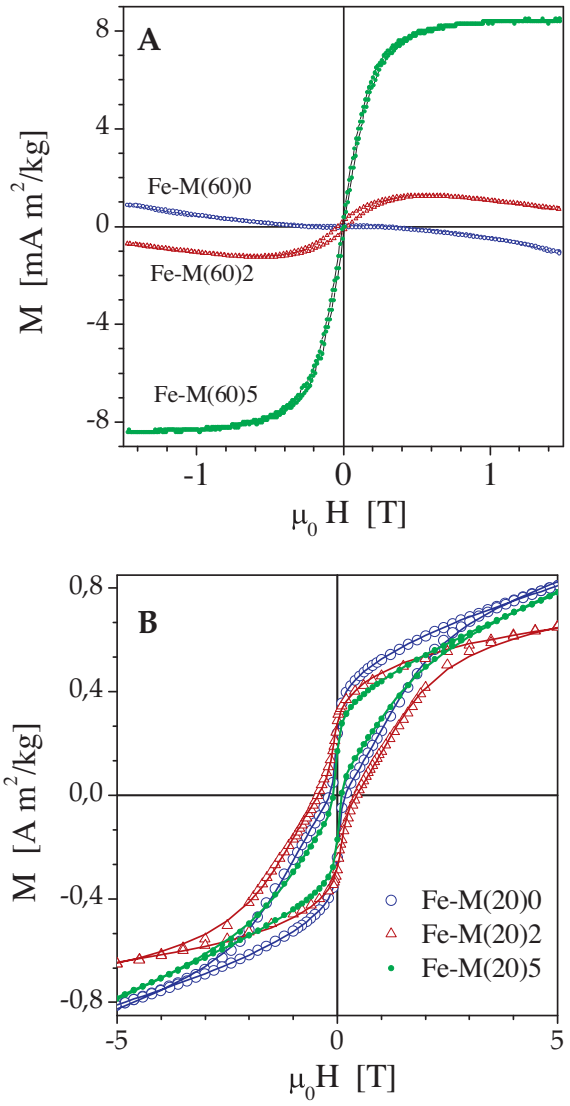

Fig. 3. Magnetization curves of samples synthesized with different hydrothermal treatment times and Si/Fe molar ratio of: (A) 60 (~1.12 wt.%) and (B) 20 (~4.2 wt.%). Symbols: experimental data; solid lines: fitting curves.

hysteresis loops have, besides the lineal contribution, superparamagnetic and ferromagnetic contributions as illustrated in Fig. 3B. These results are consistent with the increased presence of larger iron oxide nanoparticles (such as α-Fe_2O_3 and γ-Fe_2O_3), likely located on the external surface. It is important to note that although the bulk γ-Fe_2O_3 is converted to α-Fe_2O_3 above 350 °C, the presence of maghemite in our samples cannot be excluded due to its probable stabilization on the silicate matrix [59]. Taking account that γ-Fe_2O_3 and α-Fe_2O_3 nanoparticles with sizes up to ~10 nm are superparamagnetic at room temperature [58–61], the ferromagnetic contribution observed in our samples should arise from particles larger than 10 nm. However, XRD analysis did not detect iron oxide phases, probably meaning a poor crystallinity of the phases. Finally, from analysis of the fitted loops, it is possible to note that while the superparamagnetic contribution does not notably change with the thermal treatment, the ferromagnetic contribution is decreased after 5 days. This is in concordance with a decreasing in the iron species size. Thus, the results for both Fe contents are consistent with the higher stabilization of iron into the framework and the segregation of oxide species of refined sizes when the hydrothermal treatment time increases. This fact is

leading to an increased superparamagnetic contribution and/or a decreased ferromagnetic contribution.

5. Conclusions

Iron containing mesoporous silicates with MCM-41 structure and high specific surface have been prepared by directly incorporating the metallic source in the synthesis gel. The hydrothermal treatment time at 100 °C has a notable influence on the obtained mesoporous structures. While the increase in this variable negatively affects the structural regularities and area values of the materials synthesized with the lower Fe content, long synthesis times are necessary to incorporate a high Fe content reaching structures with high regularity and specific surface. Moreover, for both Fe contents studied, longer hydrothermal treatments result in a higher incorporation and stabilization of iron into the network and a refiner effect on the iron species segregated, leading to the observed superparamagnetic response. The results also show that the control of the iron precursor concentration during the first synthesis stage is important. Thus, the ferromagnetic contribution for the samples with high Fe content (Si/Fe = 20) would be arising from the increased presence of larger nanoparticles, which mainly grow on the external surface.

Acknowledgements

The authors are grateful to CONICET, UTN-FRC and FaMAF-UNC for the financial support. We are grateful to Eng. Eliana G. Vaschetto for their valuable help in experimental activities.

References

[1] D.K. Yi, S.T. Selvan, S.S. Lee, G.C. Papaefthymiou, D. Kundaliya, J.Y. Ying, J. Am. Chem. Soc. 127 (2005) 4990–4991.
[2] V. Salgueirino-Maceira, M.A. Correa-Duarte, M. Spasova, L.M. Liz-Marzan, M. Farle, Adv. Funct. Mater. 16 (2006) 509–516.
[3] K. Simeonidis, S. Mourdikoudis, M. Moulla, C. Martinez-Boubeta, M. Angelkeris, C. Dendrinou-Samara, O. Kalogirou, J. Magn. Magn. Mater. 316 (2007) e1–e4.
[4] T. Sen, A. Sebastianelli, I.J. Bruce, J. Am. Chem. Soc. 128 (2006) 7130–7131.
[5] J. Zhang, W. Sun, L. Bergman, J. Rosenholm, M. Lindén, G. Wu, H. Xu, H. Gu, Mater. Lett. 67 (2012) 379–382.
[6] T.R. Sathe, A. Agrawal, S. Nie, Anal. Chem. 78 (2006) 5627–5632.
[7] C.S. Kumar, J. Hormes, C. Leuschner, Nanofabrication Towards Biomedical Applications, in: Wiley-VCH, Weinheim, 2005.
[8] S. Mornet, S. Vasseur, F. Grasset, E.J. Duguet, J. Mater. Chem. 14 (2004) 2161–2175.
[9] J. Won, M. Kim, Y.-W. Yi, Y.H. Kim, N. Jung, T.K. Kim, Science 309 (2005) 121–125.
[10] S. Laurent, S. Dutz, U. Häfeli, M. Mahmoudi, Adv. Colloid Interface Sci. 166 (2011) 8–23.
[11] H. Xua, Z. Aguilar, L. Yang, M. Kuang, H. Duan, Y. Xiong, H. Wei, A. Wang, Biomaterials 32 (2011) 9758–9765.
[12] D.L. Huber, Small 1 (2005) 482–501.
[13] T. Tsonchevaa, J. Roggenbuck, D. Paneva, M. Dimitrov, I. Mitov, M. Fröba, Appl. Surf. Sci. 257 (2010) 523–530.
[14] C.T. Kresge, M.E. Leonowicz, W.J. Roth, J.C. Vartuli, J.S. Beck, Nature 359 (1992) 710–712.
[15] J.S. Beck, J.C. Vartuli, W.J. Roth, M.E. Leonowicz, C.T. Kresge, K.T. Schmitt, C.T.-W. Chu, D.H. Olson, E.W. Sheppard, S.B. McCullen, J.B. Higgins, J.L. Schlenker, J. Am. Chem. Soc. 114 (1992) 10834–10843.
[16] C.Y. Lai, B.G. Trewyn, D.M. Jeftinija, K. Jeftinija, S. Xu, S. Jeftinija, V.S.Y. Lin, J. Am. Chem. Soc. 125 (2003) 4451–4459.
[17] K.Y. Ho, G. McKay, K.L. Yeung, Langmuir 19 (2003) 3019–3024.
[18] A. Sayari, S. Hamoudi, Y. Yang, Chem. Mater. 17 (2005) 212–216.
[19] B. Lee, H.J. Im, H.M. Luo, E.W. Hagaman, S. Dai, Langmuir 21 (2005) 5372–5376.
[20] S.B. Wang, H.T. Li, Microporous Mesoporous Mater. 97 (2006) 21–26.
[21] M. Vallet-Regi, F. Balas, D. Arcos, Angew. Chem. Int. Ed. 46 (2007) 754875–754958.
[22] N.E. Botterhuis, Q. Sun, P.C.M.M. Magusin, R.A. Santen, N.A.J.M. Sommerdijk, Chem. Eur. J. 12 (2006) 1448–1456.
[23] H.J. Kim, J.E. Ahm, S. Haam, Y.G. Shul, S.Y. Song, T.J. Tatsumi, J. Mater. Chem. 16 (2006) 1617–1621.
[24] E. Ruiz-Hernandez, A. Lopez-Noriega, D. Arcos, I. Izquierdo-Barba, O. Terasaki, M. Vallet-Regi, Chem. Mater. 19 (2007) 34553463.
[25] R. Xing, H. Lin, F. Qu, Colloids Surf. A: Physicochem. Eng. Aspects (2010), http://dx.doi.org/10.1016/j.colsurfa.2012.03.017.
[26] Q. He, J. Shi, F. Chen, M. Zhu, L. Zhang, Biomaterials 31 (2010) 3335–3346.
[27] Q. Gan, X. Lu, Y. Yuan, J. Qian, H. Zhou, X. Lu, J. Shi, C. Liu, Biomaterials 32 (2011) 19321942.
[28] P. Wang, Y. Zhu, X. Yang, C. Li, Colloids Surf. A 294 (2007) 287–291.
[29] R.S. Prakasham, G.S. Devi, K.R. Laxmi, Ch.S. Rao, J. Phys. Chem. C 111 (2007) 3842–3847.
[30] H.H.P. Yiu, S.C. McBain, A.J. ElHaj, J. Dobson, Nanotechnology 18 (2007) 435601–435607.
[31] K.C. Souza, G. Salazar-Alvarez, J.D. Ardisson, W.A.A. Macedo, E.M.B. Sousa, Nanotechnology 19 (2008) 185603–185610.
[32] M. Liong, J. Lu, M. Kovochich, T. Xia, S.G. Ruehm, A.E. Nel, F. Tamanoi, J.I. Zink, ACS Nano 2 (2008) 889–896.
[33] S. Guo, D. Li, L. Zhang, J. Li, E. Wang, Biomaterials 30 (2009) 1881–1889.
[34] D.K. Yi, S.S. Lee, G.C. Papaefthymiou, J.Y. Ying, Chem. Mater. 18 (2006) 614–619.
[35] J. Yu, H. Zhao, L. He, H. Yang, S. Ku, N. Yang, N. Xiao, J. Mater. Chem. 19 (2009) 1265–1270.
[36] E. Ruiz-Hernández, A. López-Noriega, D. Arcos, M. Vallet-Regí, Solid State Sci. 10 (2008) 421–426.
[37] L. Guo, J. Li, L. Zhang, J. Li, Y. Li, C. Yu, J. Shi, M. Ruan, J. Feng, J. Mater. Sci. 18 (2008) 2733–2738.
[38] S. Zhu, Z. Zhou, D. Zhang, C. Jin, Z. Li, Microporous Mesoporous Mater. 106 (2007) 56–61.
[39] L. Qu, S. Tie, Microporous Mesoporous Mater. 117 (2009) 402–405.
[40] M. Asada, Y. Hara, Y. Kuroda, S. Tanaka, T. Horikawa, Y. Miyake, Ind. Eng. Chem. Res. 48 (2009) 2577–2582.
[41] Z. Surowiec, B. Bierska-Piech, M. Wiertel, M. Budzynski, J. Goworek, Acta Phys. Polon. A 114 (6) (2008) 1605.
[42] S. Alam, C. Anand, R. Logudurai, V. Balasubramanian, K. Ariga, A. Chandra Bose, T. Mori, P. Srinivasu, A. Vinu, Microporous Mesoporous Mater. 121 (2009) 178–184.
[43] Y. Zhu, S. Kaskel, T. Ikoma, N. Hanagata, Microporous Mesoporous Mater. 123 (2009) 107–112.
[44] M. Morales, A. Mascarenhas, A. Gomes, C. Leite, H. Andrade, C. de Castilho, F. Galembeck, J. Colloids Interface. Sci. 342 (2010) 269–277.
[45] M. Stearns, Y. Cheng, J. Appl. Phys. 75 (1994) 6894–6898.
[46] P. Allia, M. Coisson, M. Knobel, P. Tiberto, F. Vinai, Phys. Rev. B. 60 (1999) 12207–12218.
[47] V.R. Elías, M.I. Oliva, S.E. Urreta, S.P. Silvetti, K. Sapag, A.M. Mudarra Navarro, S.G. Casuscelli, G.A. Eimer, Appl. Catal. A: Gen. 381 (2010) 92–100.
[48] X.-Y. Hao, Y.-Q. Zhang, J.-W. Wang, W. Zhou, C. Zhang, S. Liu, Microporous Mesoporous Mater. 88 (2005) 38–47.
[49] H.T. Gomes, P. Selvam, S.E. Dapurkar, J.L. Figueiredo, J.L. Faria, Microporous Mesoporous Mater. 86 (2005) 287–294.
[50] G.A. Eimer, C.M. Chanquía, M.S. Sapag, E.R. Herrero, Microporous Mesoporous Mater. 116 (2008) 670–676.
[51] S.G. Aspromonte, A. Sastre, A.V. Boix, M.J. Cocero, E. Alonso, Microporous Mesoporous Mater. 148 (2012) 53–61.
[52] Y. Lu, J. Zheng, J. Liu, J. Mu, Microporous Mesoporous Mater. 106 (2007) 28–34.
[53] Y. Wang, Q. Zhang, T. Shishido, K. Takehira, J. Catal. 209 (2002) 186–196.
[54] A. De Stefanis, S. Kaciulis, L. Pandolfi, Microporous Mesoporous Mater. 99 (2007) 140–148.
[55] L. Shiquan, Q. Wang, P. Van Der Voort, P. Cool, J. Magn. Magn. Mater. 280 (2004) 31–36.
[56] L. Chmielarz, P. Kustrowski, R. Dziembaj, P. Cool, E. Vansant, Appl. Catal. 62 (2006) 369–380.
[57] D. Beydoun, R. Amal, G. Low, S. MacEvoy, J. Nanopart. Res. 1 (1999) 439–458.
[58] R. Cornell, U. Schwertmann, The Iron Oxides: Structures, Properties, Reactions, Occurrences and Uses, Wiley-VCH, Weinheim, 2003.
[59] Y. Wang, J. Ren, X. Liu, Y. Wang, Y. Guo, Y. Guo, G. Lu, J. Colloids Interface Sci. 326 (2008) 158–165.
[60] S. Liu, Q. Wang, P. Van Der Voort, P. Cool, E. Vansant, M. Jiang, J. Magn. Magn. Mater. 280 (2004) 31–36.
[61] J. Jung, K. Choi, Y. Jung, S. Lee, V. Golub, L. Malkinski, C. O'Connor, J. Magn. Magn. Mater. 272-276 (2004) e1157–e1159.